Controllable Spin−Orbit Torque Induced by Interfacial Ion Absorption in Ta/CoFeB/MgO Multilayers with Canted Magnetizations

Jingyan Zhang,[†] Yunchi Zhao,[†] Pengwei Dou, Wenlin Peng, He Huang, Xiao Deng, Yuanbo Wang, Jialong Liu, Jiawang Xu, Tao Zhu, Jie Qi, Xinqi Zheng, Yanfei Wu, Baogen Shen, and Shouguo Wang*

Cite This: *ACS Appl. Mater. Interfaces* 2023, 15, 49902−49910
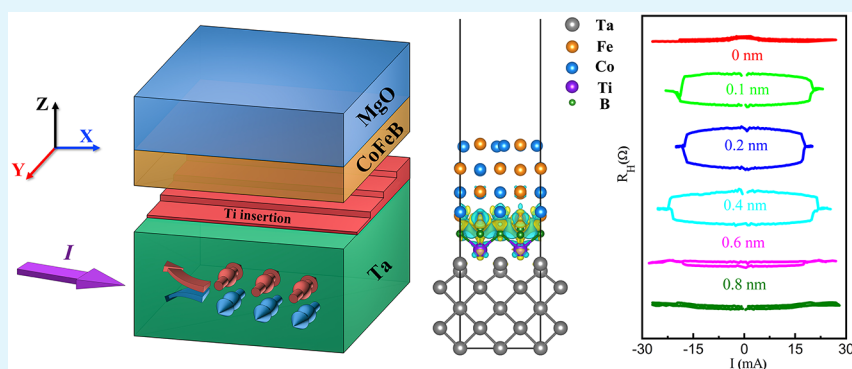
Read Online

ACCESS | Metrics & More | Article Recommendations | Supporting Information

ABSTRACT: Electrically generated spin−orbit torque (SOT) has emerged as a powerful pathway to control magnetization for spintronic applications including memory, logic, and neurocomputing. However, the requirement of external magnetic fields, together with the ultrahigh current density, is the main obstacle for practical SOT devices. In this paper, we report that the field-free SOT-driven magnetization switching can be successfully realized by interfacial ion absorption in perpendicular Ta/CoFeB/MgO multilayers. Besides, the tunable SOT efficiency exhibits a strong dependence on interfacial Ti insertion thicknesses. Polarized neutron reflection measurements demonstrate the existence of canted magnetization with Ti inserted, which leads to deterministic magnetization switching. In addition, interfacial characterization and first-principles calculations reveal that B absorption by the Ti layer is the main cause behind the enhanced interfacial transparency, which determines the tunable SOT efficiency. Our findings highlight an attractive scheme to a purely electric control spin configuration, enabling innovative designs for SOT-based spintronics via interfacial engineering.

KEYWORDS: spin−orbit torque, deterministic magnetization switching, interfacial ion absorption, spin transparency, canted magnetization

INTRODUCTION

Spinorbit torque (SOT) enables the electric manipulation of the spin configuration for implementing energy-efficient spintronic integration.[1−8] Currently, SOT-driven systems have been widely explored in many respects, involving magnetization switching,[9,10] domain wall motion,[11,12] magnetic oscillation excitation,[13,14] and so on.[15−19] For a SOT-based storage cell, the key point is to realize field-free SOT-driven magnetization switching in a heavy metal/ferromagnet (HM/FM) heterostructure.[20] Up to now, it was demonstrated that SOT-driven magnetization switching can be tuned by an engineering interfacial or interlayer exchange interaction.[21−25] Furthermore, inhomogeneous magnets mainly including a structure/component gradient have been successfully fabricated to achieve deterministic magnetization switching.[26−29] Especially, symmetry-dependent field-free magnetization

switching was observed in an epaxial CuPt/CoPt bilayer due to an interfacial low-symmetry point group.[30] In addition, the electric-control method has also been used to manipulate the SOT efficiency to realize field-free switching.[4,31,32] In general, an enhanced SOT efficiency results in a low critical current density. The SOT efficiency per unit of current density (ξ_{SH}) can be characterized as $\xi_{SH} = T_{int}\theta_{SH}$, where θ_{SH} is the internal spin Hall angle (SHA) and T_{int} is the interfacial spin
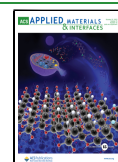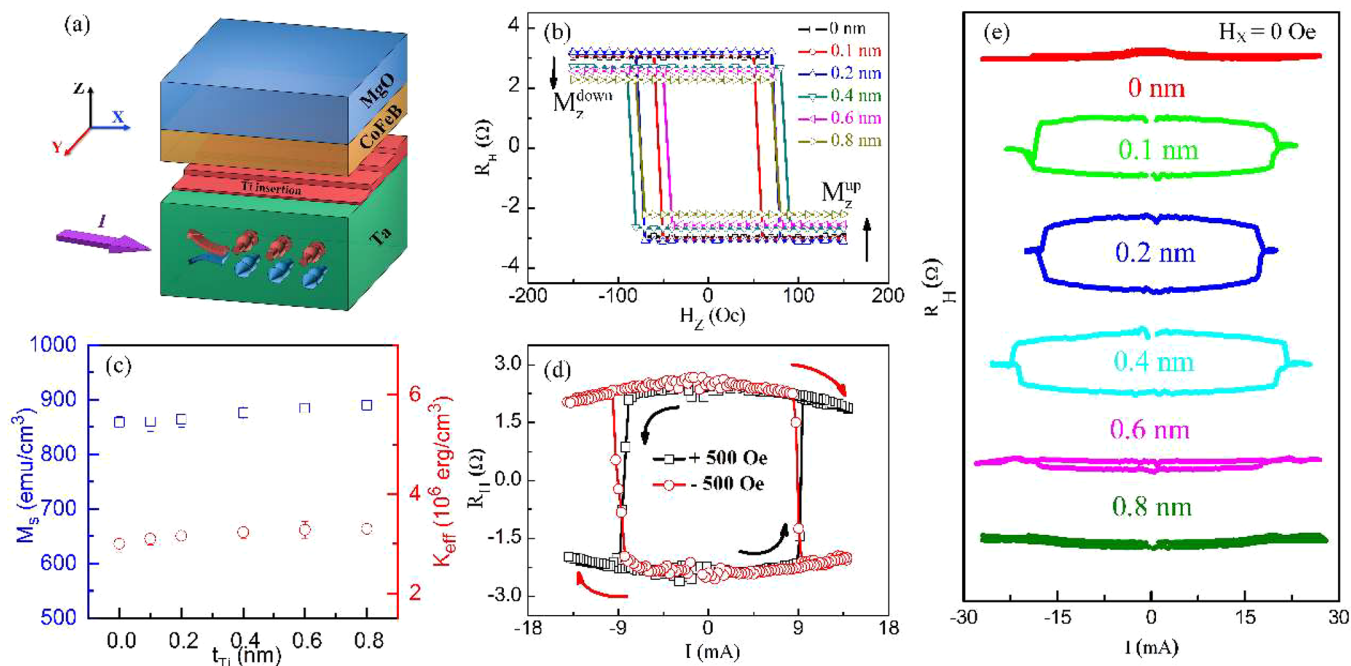
Figure 1. (a) Schematic of the Ta/CoFeB/MgO multilayers. (b) Hall loops for the samples with various Ti insertion thicknesses (t_{Ti}). (c) M_s and K_{eff} as functions of t_{Ti}, respectively. (d) SOT-driven magnetization switching loops under ±500 Oe. (e) $R-I$ curves under the absence of an external field for samples with various t_{Ti}.

transparency.[13,14] Extensive efforts have been paid to exploring new HM materials with large θ_{SH} values to realize the SOT behavior.[33−39]

The Ta/CoFeB/MgO structure is one of the promising candidates in the area of SOT-based high-density memories because of its robust perpendicular magnetic anisotropy (PMA), which is essential to maintaining a large energy barrier against thermal fluctuation.[40] Unfortunately, the intermixing between Ta and the CoFeB layer during thermal annealing impedes the transmittance of spin current, which will greatly degrade ξ_{SH}.[41] Meanwhile, T_{int} has been theoretically demonstrated to be strongly dependent on the HM/FM interfacial structure.[42,43] Recently, a submonolayer Ti layer was used to modify the bulk Pt spin source ($[Pt/Ti]_n$ multilayers).[44,45] However, little experimental evidence for tunable T_{int} on field-free SOT-driven magnetization switching has been found up to now. Here, field-free SOT-driven magnetization switching and a tunable SOT efficiency can be simultaneously achieved in perpendicular Ta/CoFeB/MgO multilayers by introducing atomic-scale Ti layers at the Ta/CoFeB interface. According to interfacial characterization, together with first-principles calculations, the above results should be attributed to the interfacial canted magnetization and enhanced spin transparency induced by interfacial Ti insertion.

■ EXPERIMENTAL METHODS

Multilayers consisting of Ta(5)/Ti(t_{Ti})/Co$_{40}$Fe$_{40}$B$_{20}$(1)/MgO(2)/Cu(1) (in nanometers) were deposited on thermally oxidized Si wafers at room temperature using a magnetron sputtering system (AJA, ATC-2200UHV). More details about film growth can be found elsewhere.[10,46] After growth, the films were annealed at 300 °C for 35 min using a vacuum annealing furnace (F800-35, East Changing Technologies, China). Subsequently, Hall bar devices were fabricated by ultraviolet lithography and ion-beam etching for magnetoelectric transport measurements, and contact pads made of Cr(5)/Au(65) (in nanometers) were additionally deposited as electrodes. A Keithley

6221 current source and a 2182A nanovoltmeter were used, where a direct current was applied. During current-driven magnetization switching, different pulses with a duration of 200 μs were applied using the current source. After 10 s, a small direct current (500 μA) as an excitation current was applied to eliminate the thermal effect, while a 2182A nanovoltmeter was used to record the Hall voltage at each point. For harmonic measurements, two SR830 lock-in amplifiers were employed to record the first- and second-harmonic Hall voltages. To ensure the accuracy of the experimental results, four samples or Hall bars were carefully measured during the magnetoelectric-transport measurement. Energy-dispersive X-ray spectroscopy (EDS) spectra were obtained using a spherical aberration-corrected FEI Themis Z microscope. Interfacial states were characterized using X-ray photoelectron spectroscopy (XPS, ESCALAB 250Xi) and a high-resolution X-ray reflection system (XRR, Bruker D8). The Dzyaloshinskii−Moriya interaction (DMI) constant was obtained using Brillouin light scattering (BLS) spectroscopy. Polarized neutron reflection (PNR) measurements were performed by using the Multipurpose Reflectometer at the China Spallation Neutron Source. All density functional theory calculations in this work were performed by the Vienna Ab Initio Simulation Package (VASP) software.[47] When the projector-augmented-wave algorithm was employed, the electronic exchange-correlation interactions were described using the generalized gradient approximation with the Perdew−Burke−Ernzerhof functional.[48−50]

■ RESULTS AND DISCUSSION

Figure 1a presents a schematic of multilayers under the orthogonal coordinate system. In this study, a current was applied through the main channel along the X axis. First, the anomalous Hall resistance (R_H) was measured in the multilayers. Figure 1b shows Hall loops for samples with various Ti thicknesses (t_{Ti}). Sharp square loops can be observed, suggesting good PMA in all samples with various t_{Ti} values. The R_H value is 2.9 Ω for the sample without Ti insertion, and a slight enhancement of R_H can be obtained for 0.1 nm Ti insertion (3.0 Ω) and 0.2 nm Ti insertion (3.1 Ω). With further increasing t_{Ti}, the R_H value significantly decreases

($R_H \sim 2.2\ \Omega$) due to a shunting effect when t_{Ti} is 0.8 nm. In general, the anomalous Hall effect in FMs originates from spin−orbit coupling (SOC), leading R_H to be proportional to saturation magnetization (M_s). In addition to M_s, spin-dependent scattering at interfaces also plays a crucial role in tuning R_H in a multilayered structure. Figure 1c presents M_s and the effective magnetic anisotropy constant (K_{eff}) as functions of t_{Ti}, respectively. It shows a slight change in the M_s value with increasing t_{Ti}. Meanwhile, the value of K_{eff} is 3×10^6 erg/cm^3 for the sample without insertion, and it reaches 3.3×10^6 erg/cm^3 for the sample with 0.8 nm Ti insertion, suggesting the same tendency in K_{eff}−t_{Ti} curves. To avoid the joule heating effect, a pulse current was applied to investigate SOT-driven magnetization switching. Figure 1d presents R−I loops for Ta/CoFeB/MgO multilayers with assisted magnetic fields (H_X) of ±500 Oe. Full magnetization switching can be clearly observed under assisted H_X when $t_{Ti} = 0$. The reversal of the switching polarity takes place when the H_X direction is changed from the +X to −X axis, consistent with the previous study.[51] Generally, deterministic magnetization switching under the absence of H_X is the most attractive for practical applications of the SOT-based device. Figure 1e presents field-free SOT-driven magnetization switching loops for samples with various t_{Ti}. As expected, nearly no magnetization switching can be observed under zero fields in the sample without Ti insertion. It is worth emphasizing that field-free magnetization switching can be successfully realized in the sample with ultrathin Ti insertion ($0 < t_{Ti} \leq 0.4$ nm). With further increasing t_{Ti}, no obvious magnetization switching behavior can be achieved, indicating various deterministic magnetization switching behaviors via t_{Ti}. More details on SOT-driven magnetization switching can be found in Figure S1. The minimum critical current density of 2.7×10^7 A/cm^2 was obtained in the sample with 0.2 nm Ti insertion (Figure S1a). Therefore, it is reasonable to conclude that ultrathin Ti insertion plays an obvious role in SOT-driven magnetization switching.

In general, SOTs, mainly including damping-like (DL) and field-like (FL) torques, give rise to magnetization dynamics.[52,53] Hence, harmonic measurements were performed to check the spin torques. First, the spin torque from Ti insertion should be carefully verified. Samples with the structures of Ti(5)/CoFeB(1)/MgO(2)/Cu(1) (denoted as the Ti/CFB sample) and Ta(5)/CoFeB(1)/MgO(2)/Cu(1) (denoted as the Ta/CFB sample) (in nanometers) were prepared. Parts a and b of Figure 2 show second-harmonic voltage ($V_{2\omega}$) as a function of H_x (parallel) and H_y (perpendicular) for the above two samples, respectively. When H_y is swept from +5000 to −5000 Oe, the $V_{2\omega}$−H_y loop for the Ta/CFB sample shows a negative peak, indicating a negative SHA in Ta. The effective SHA is estimated to be 0.08 in our reference sample Ta/CoFeB/MgO. Furthermore, the $V_{2\omega}$ value of the Ti/CFB sample is far less than that of the Ta/CFB sample shown in Figure 2. According to the negligible $V_{2\omega}$ signal, the spin torque from the Ti layer can be neglected, in good agreement with the previous study.[54] In addition, the ultrathin Ti insertion ($t_{Ti} < 1$ nm) at the interface cannot generate a considerable orbital torque, which was confirmed in the recent study.[55] Second, the damping-like (H_{DL}) and field-like (H_{FL}) effective fields should be measured in the samples with various t_{Ti} (Figure S2). Figure 2c displays the damping-like effective field strength (β_{DL}) of both magnetization states (+M and −M) as a function of t_{Ti} for Ta/Ti(t_{Ti})/CoFeB/MgO
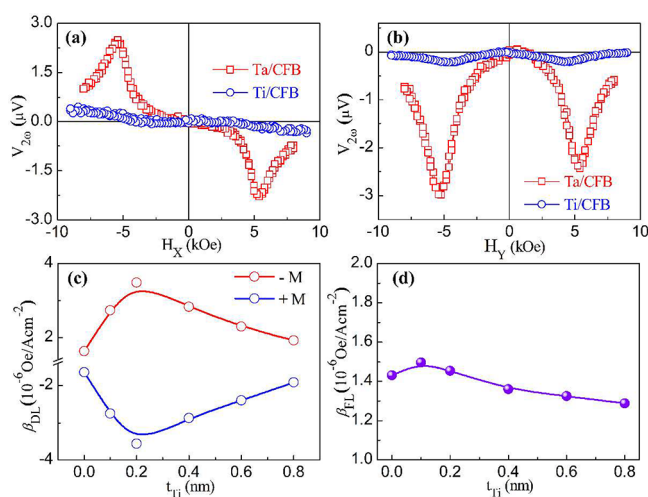

Figure 2. (a and b) $V_{2\omega}$ as a function of H_x (parallel) and H_y (perpendicular) in the current direction for Ta(5 nm)/CoFeB/MgO and Ti(5 nm)/CoFeB/MgO multilayers, respectively. (c and d) β_{DL} and β_{FL} as a function of t_{Ti}, respectively.

multilayers. It shows a nonlinear relationship between β_{DL} and t_{Ti}. For the −M state, when $t_{Ti} = 0.2$ nm, the β_{DL} value of 3.52×10^{-6} Oe/A·cm^{-2} reaches a maximum value, which is 2.15 times as much as that in the sample without Ti insertion (1.64×10^{-6} Oe/A·cm^{-2}). The tendency is consistent with the J_{sw}−t_{Ti} curve shown in Figure S1a, indicating a maximum damping-like torque in the sample with 0.2 nm Ti insertion. Figure 2d presents the thickness dependence of the field-like effective field strength (β_{FL}). A slight change in the β_{FL} value can be observed with increasing t_{Ti}. For example, the β_{FL} values are 1.43×10^{-6} and 1.49×10^{-6} Oe/A·cm^{-2} for the samples with no and 0.2 nm Ti insertion, respectively. This suggests that tunable damping-like torque plays a dominant role in the SOT behavior.

The elemental composition change was characterized by high-resolution scanning transmission electron microscopy and EDS (Figure S3). The Mg, Co, Fe, and Ta elements can be detected; however, the Ti signal is very weak due to the ultrathin thickness. XPS, together with Ar$^+$ ion etching, provides an effective means to detect relatively few elements and their depth distribution.[56] Mg 1s was selected as a reference to identify the etching depth (Figure S4). The Mg 1s peak appears when the Ar$^+$ etching time is 10 s. Furthermore, the intensity significantly decreases for 30 s and then disappears for 40 s. This indicates that the depth of Ar$^+$ etching extends to the CoFeB layer when the etching time is beyond 30 s. The samples with no and 0.2 nm Ti insertion were marked as S−O and S−T, respectively. Parts a and b of Figure 3 present Ta 4f high-resolution XPS spectra for S−O and S−T, respectively. For the sample S−O with 10 s Ar$^+$ etching in Figure 3a, peaks 1 and 2 located at 22.1 and 24.0 eV correspond to Ta $4f_{7/2}$ and $4f_{5/2}$ in metallic Ta, respectively, and peaks 3 and 4 located at 26.4 and 28.3 eV correspond to Ta $4f_{7/2}$ and $4f_{5/2}$ in Ta$_2$O$_5$, respectively. It indicates that Ta diffused into the MgO layer and was oxidized into Ta$_2$O$_5$, in agreement with the previous study.[57] For the sample S−T in Figure 3b, the Ta 4f peak cannot be observed with an etching time of 10 s compared with the sample S−O, suggesting that Ta diffusion was effectively suppressed by inserting a Ti layer. Parts c and d of Figure 3 present B 1s high-resolution XPS spectra for the samples S−O and S−T, respectively. For the
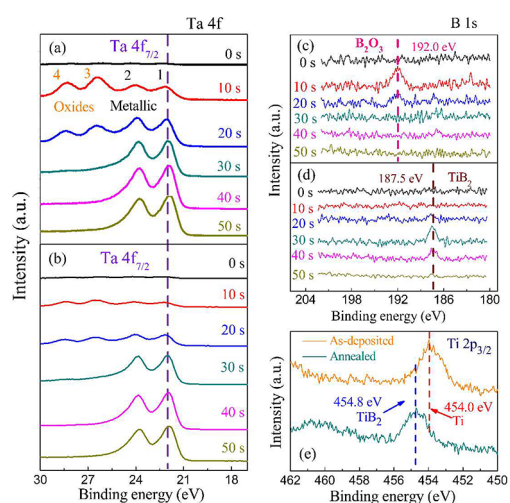
Figure 3. Ta 4f high-resolution XPS spectra for the sample (a) without insertion and (b) with 0.2 nm Ti insertion, respectively. B 1s high-resolution XPS spectra for the sample (c) without insertion and (d) with 0.2 nm Ti insertion, respectively. (e) Ti 2p high-resolution XPS spectra with an Ar^+ etching time of 30 s for the sample with 0.2 nm Ti insertion at as-deposited and annealed states, respectively.

sample S−O in Figure 3c, the B 1s peak appears when the etching time reaches 10 s, suggesting that the B atom diffuses

into the CoFeB/MgO interface. The B 1s peak disappears with increasing etching time to 30 s. The peak located at 192.0 eV shown in Figure 3c corresponds to B^{3+} in B_2O_3. For the sample S−T in Figure 3d, the B 1s peak appears until the etching time is up to 30 s. The B 1s peak located at 187.5 eV corresponds to the B^- state, reflecting a shift of 4.5 eV toward lower binding energy compared with the sample S−O. In addition, Ti 2p high-resolution XPS spectra are presented in Figure 3e for the as-deposited and annealed S−T with an etching time of 30 s, respectively. For as-deposited S−T, the Ti $2p_{3/2}$ peak located at 454.0 eV corresponds to Ti^0 in metallic Ti. Obviously, the Ti $2p_{3/2}$ peak located at 454.8 eV for the annealed S−T corresponds to the Ti^{2+} state, which shows a shift of 0.8 eV toward higher binding energy. Therefore, it is reasonable to conclude that interfacial TiB_2 is formed by introducing an ultrathin Ti insertion at the Ta/CoFeB interface.

Parts a and b of Figure 4 show the specular XRR profiles for the samples without and with 0.2 nm Ti insertion, respectively. *Leptos*7 software was used to analyze the XRR data. XRR curves were fitted using the simplex method to obtain the Ta/CoFeB interfacial roughness (Tables S1 and S2). For the sample without insertion in Figure 4a, the interfacial roughness is 0.11 and 0.38 nm for the as-deposited and annealed states, respectively. The remarkable increment should be due to Ta diffusion. For the sample with 0.2 nm Ti insertion in Figure 4b, the interfacial roughness is 0.19 nm for the as-deposited state,
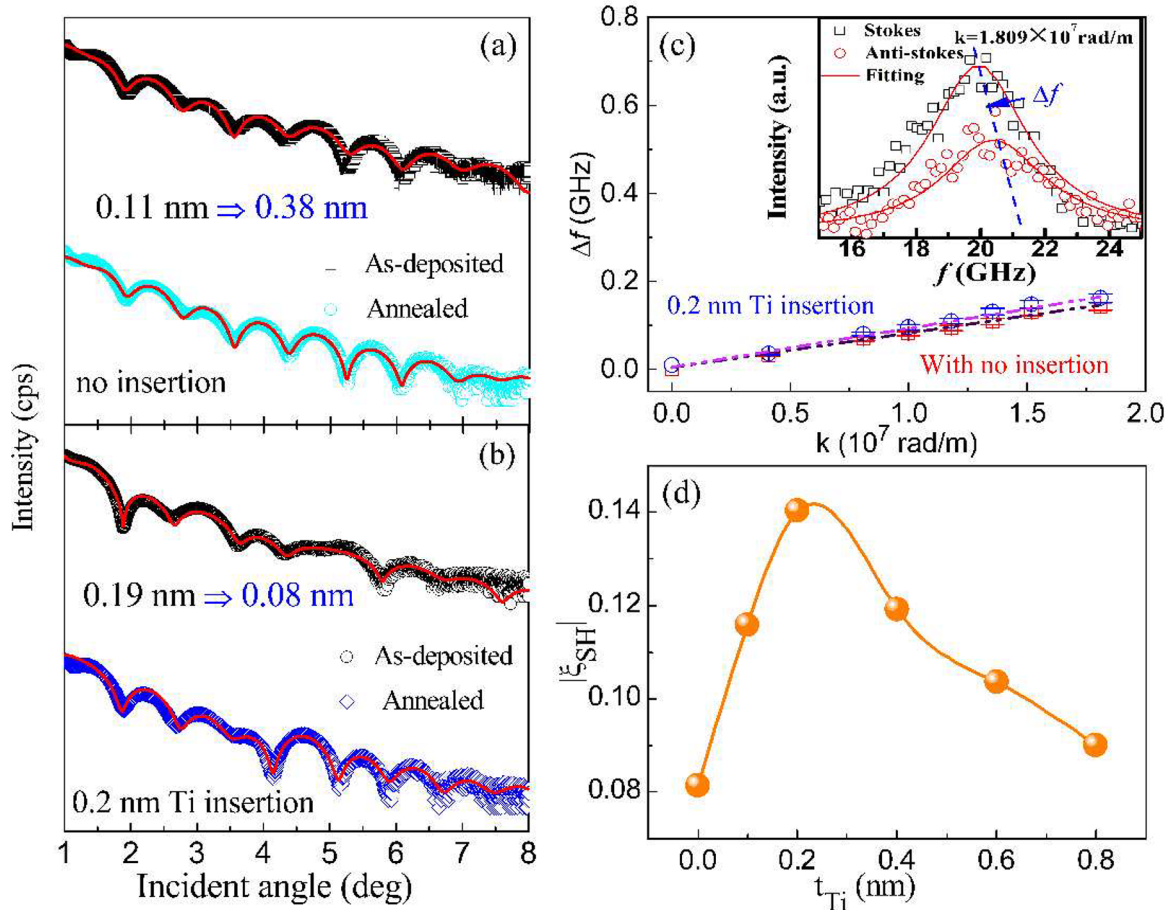

Figure 4. (a and b) Specular XRR profiles for the sample without and with 0.2 nm Ti insertion at the as-deposited and annealed states, respectively. (c) Δf as a function of k for the sample without and with 0.2 nm Ti insertion. BLS spectra recorded at a fixed incident angle $k = 1.809 \times 10^7$ rad/m in the sample without insertion are shown in the inset. (d) Absolute value of ξ_{SH} as a function of t_{Ti}.
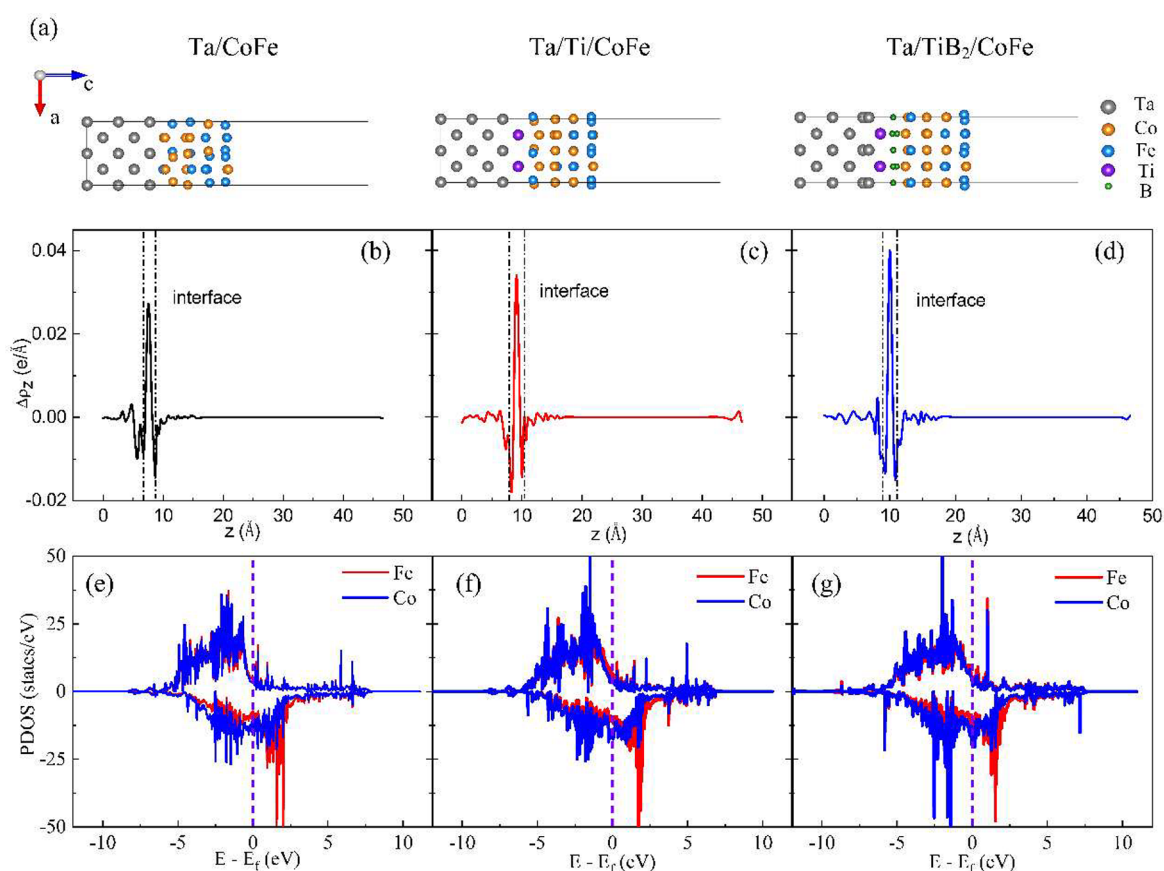
Figure 5. (a) Optimized atomic configurations of the Ta/CoFe, Ta/Ti/CoFe, and Ta/TiB$_2$/CoFe heterostructure slab models. (b−d) Corresponding $\Delta\rho_z$ values of the Ta/CoFe, Ta/Ti/CoFe, and Ta/TiB$_2$/CoFe heterostructure slabs along the z axis. The positive values indicate electron accumulation, and the negative values indicate electron depletion. (e−g) Spin-up and spin-down PDOSs of Fe and Co in the Ta/CoFe, Ta/Ti/CoFe, and Ta/TiB$_2$/CoFe heterostructure slabs. The Fermi-energy level is set to zero.

and it significantly decreases to 0.08 nm for the annealed state. According to the XRR results, this suggests that improvement of the interfacial structure can be obtained by introducing an ultrathin Ti insertion. In addition, the SOT behavior can be remarkably affected by interfacial DMI.[58,59] To quantify the interfacial DMI constant (D), momentum (k)-resolved BLS measurements were performed by changing the incident angle for our samples. The D value can be calculated based on eq 1[60]

$$\Delta f = \frac{2\gamma}{\pi M_s} D k \qquad (1)$$

where γ and M_s are the gyromagnetic ratio and saturated magnetization of the CoFeB layer, respectively. Δf can be calculated by the interpolation between the Stokes and anti-Stokes peak locations in the inset of Figure 4c. Figure 4c shows the Δf value as a function of k. The values of D are 0.055 and 0.067 mJ/m^2 for samples without and with 0.2 nm Ti insertion, respectively, indicating a slight enhancement of interfacial DMI via insertion of the Ti layer. In general, DMI at the HM/FM interface plays a crucial role in stabilizing the Néel-type domain walls with certain chirality.[61] Enhanced DMI gives rise to a higher barrier of SOT-driven magnetization switching, leading to the requirement of larger assisted magnetic fields.[62] Therefore, the effect of DMI on SOT-driven magnetization switching should be excluded. Figure 4d presents the absolute value of the SOT efficiency (ξ_{SH}) as a function of t_{Ti}. ξ_{SH} can be determined using the following equation:[63]

$$\xi_{SH} = \frac{2e}{\hbar} \mu_0 M_s t_F \frac{\Delta H_{DL}}{j_e} \qquad (2)$$

where t_F is the thickness of the ferromagnetic layer. Although both the M_s and K_{eff} values slightly change via t_{Ti} shown in Figure 1, this shows the nonlinear change of the ξ_{SH} value with increasing t_{Ti}. The maximum value of ξ_{SH} reaches 0.14 in the sample with 0.2 nm Ti insertion, which is 75% larger than that of the sample without Ti insertion.

In addition, interfacial electronic interactions at the Ta/CoFeB interface were investigated to gain insight into the modified interfacial structure using first-principles calculations. The model and schematic of the Ta/CoFeB interface are presented in Figure 5a. When an interfacial Ti layer was introduced considering the individual Ti and corresponding TiB$_2$ thin-film formation after annealing, the CoFe lattice distortion was suppressed, indicating good structural stability and interfacial adaptation. Parts b−d of Figure 5 show the planar charge-density differences ($\Delta\rho_z$) integrated along the perpendicular direction of the heterostructures for the three types of interfaces. Compared with $\Delta\rho_z$ at the Ta/CoFe interface (0.027 e/Å), significantly higher interfacial electron accumulations with maximum values of 0.034 and 0.040 e/Å for the interface with Ti and TiB$_2$ insertion, respectively, were obtained. Furthermore, the partial densities of states (PDOSs) of Fe and Co in the corresponding Ta/CoFe, Ta/Ti/CoFe, and Ta/TiB$_2$/CoFe interfaces were calculated to identify the electronic behavior differences near the Fermi surface. As

depicted in Figure 5e−g, the absolute values of the PDOS near the Fermi energy (E_f) level become larger with insertion of Ti and the TiB$_2$ layer, leading to increased concentration of free conduction electrons and promoting a higher electronic conduction ability. Notably, enhancement of the spin-down PDOS of Co and Fe can be found in Figure 5f,g, indicating the selective excitation of spin polarization at the HM/FM interface. Therefore, the calcuation results show that enhanced electron transport and interfacial transparency can be achieved by introducing atomic Ti and TiB$_2$ insertion.

For the HM/FM/oxide trilayered structure, the ξ_{SH} value was determined by two components: θ_{SH} and T_{int}. The θ_{SH} value has a linear change with the electrical resistivity (ρ_{xx}), which can be expressed by the equation[64]

$$\theta_{SH} = (2e/\hbar)\sigma_{SH}\rho_{xx} \qquad (3)$$

In this study, the ρ_{xx} value in the multilayers monotonously decreases with increasing t_{Ti} (Figure S5). Therefore, the ξ_{SH} tendency cannot be explained by the θ_{SH} change. Moreover, the change of $\Delta\rho_z$ and PDOS demonstrated by the first-principles calculations results in Figure 5 reveals enhancement of the electron conductivity and spin polarization at the interface, indicating the realization of higher T_{int}. Our focus will be on T_{int}. According to the interfacial analysis, the B ion absorption by the Ti layer forms an interfacial TiB$_2$ barrier, which suppresses the Ta and B atom diffusion to determine low interface roughness. TiB$_2$ with a hexagonal AB$_2$ structure, where B atoms can form strongly bonded graphene-like sheets between layers of metal atoms, was reported. The structure has good electrical conductivity as well as chemical and thermal stability.[65−67] In addition, as depicted in Figure 4d, an ultrathin Ti insertion can significantly improve the SOT efficiency, suggesting the positive effect of an improved interfacial structure on T_{int}. Furthermore, it was demonstrated theoretically that T_{int} can be affected by two factors: (1) spin backflow (SBF), whose strength depends on the spin-mixing conductance $G^{\uparrow\downarrow}$ of the interface relative to the spin conductance G_{HM} of the HM layer;[42] (2) spin memory loss (SML), which is caused by the interfacial spin scattering.[43] On the one hand, SML is induced by the loss of spin information due to the spin-flip scattering, resulting in the spin angular momentum carried by the spin current that cannot be transferred to FM.[68] For the sample with Ti insertion, the interfacial spin scattering can be decreased due to the improved Ta/CoFeB interface with various Ti insertions, resulting in a decreased SML. On the other hand, a clear interface with good crystal perfection is found to be one of the important factors for $G^{\uparrow\downarrow}$.[69] In this study, formation of the TiB$_2$ barrier leads to the clearer Ta/CoFeB interface, which gives rise to the enhancement of $G^{\uparrow\downarrow}$ and the decreased SBF. Therefore, B ion desorption by the Ti layer is a benefit of the improvement of the interfacial structure, leading to a tunable SOT switching behavior.

To further investigate the effect of B desorption by the Ti layer on the magnetic properties, PNR measurements were performed to characterize the depth distribution of the magnetic structure. In general, the tilted angle of the magnetizations can be quantitatively calibrated to confirm the spin orientation. According to the PNR result in Figure S6, the magnetic parameters are summarized in Table 1. The values of in-plane magnetization ($M_{\parallel}$) for the multilayers with no and 0.2 nm Ti insertion are 1.095 and 1.123 μ_B under 12000 Oe, respectively. When the in-plane field is decreased to 20 Oe, the values of $M_{\parallel}$ are decreased to +0.013 and −0.042 μ_B

Table 1. In-Plane Component of Magnetizations (μ_B) under Various Magnetic Fields

Ta/Ti(t$_{Ti}$)/CoFeB/MgO	12000 Oe	20 Oe	canted angle (deg)
$M_{\parallel}$, t_{Ti} = 0 nm	1.095	0.013	0.7
$M_{\parallel}$, t_{Ti} = 0.2 nm	1.123	−0.042	−2.1

for the sample with no and 0.2 nm Ti insertion, respectively. The canted angle of 0.7° is very low for the multilayers without Ti insertion, indicating typical perpendicular magnetization in conventional Ta/CoFeB/MgO multilayers. In contrast, it increases to −2.1° when a 0.2 nm Ti layer is inserted at the interface, confirming the existence of canted magnetization in the multilayers with ultrathin Ti insertion. Generally, the tilted angle of magnetization is dependent on the competition of various energies (such as interfacial magnetization anisotropy, bulk magnetization anisotropy, DMI, and so on). The difference is that a slight change of the K_{eff} value in Ta/CoFeB/MgO multilayers originates from orbital hybridization at the CoFeB/MgO interface.[40] In addition, it should be noted that oblique sputtering was used during the Ti insertion deposition in spite of rotation of the substrate, which means that the lateral inhomogeneity might be inevitably induced when the Ti insertion is relatively thin. Therefore, the field-free magnetization switching should be attributed to the canted magnetization induced by ultrathin Ti insertion.

■ CONCLUSION

In summary, SOT-driven magnetization switching in perpendicular Ta/CoFeB/MgO multilayers with atomic-scale Ti insertion was systematically investigated. Field-free magnetization switching with J_{sw} of 2.7 × 10^7 A/cm^2 can be successfully achieved in the heterostructure with 0.2 nm Ti insertion. In addition, the SOT efficiency can be effectively tuned by various interfacial insertions. According to the PNR results, the enhanced interfacial canted magnetization is verified in the multilayered structure by introducing the ultrathin Ti insertion, leading to deterministic magnetization switching. Interfacial structural characterization, together with the first-principles calculations, confirms the Ti layer, acting as a B ion absorption source (TiB$_2$ barrier), results in enhanced interfacial transparency, which facilitates the tunable SOT efficiency. Our findings deliver an effective method to design high-performance SOT-based devices and deeply understand the mechanism of electric control spin via interfacial modification.

■ ASSOCIATED CONTENT

ⓢ Supporting Information

The Supporting Information is available free of charge at https://pubs.acs.org/doi/10.1021/acsami.3c12551.

　　SOT-driven magnetization switching behavior, harmonic Hall measurements, interfacial characterization, longitudinal resistivity, XRR measurement, and PNR measurement (PDF)

■ AUTHOR INFORMATION

Corresponding Author

Shouguo Wang − *School of Materials Science and Engineering, Beijing Advanced Innovation Center for Materials Genome Engineering, University of Science and Technology Beijing, Beijing 100083, China; Anhui Key Laboratory of Magnetic*

Functional Materials and Devices, School of Materials Science and Engineering, Anhui University, Hefei 230601, China; Email: sgwang@ustb.edu.cn

Authors

Jingyan Zhang − *School of Materials Science and Engineering, Beijing Advanced Innovation Center for Materials Genome Engineering, University of Science and Technology Beijing, Beijing 100083, China;* orcid.org/0000-0003-0012-6191

Yunchi Zhao − *Beijing National Laboratory for Condensed Matter Physics, Institute of Physics, Chinese Academy of Sciences, Beijing 100190, China*

Pengwei Dou − *School of Materials Science and Engineering, Beijing Advanced Innovation Center for Materials Genome Engineering, University of Science and Technology Beijing, Beijing 100083, China*

Wenlin Peng − *School of Materials Science and Engineering, Beijing Advanced Innovation Center for Materials Genome Engineering, University of Science and Technology Beijing, Beijing 100083, China;* orcid.org/0000-0001-9334-837X

He Huang − *School of Materials Science and Engineering, Beijing Advanced Innovation Center for Materials Genome Engineering, University of Science and Technology Beijing, Beijing 100083, China;* orcid.org/0000-0003-1335-3174

Xiao Deng − *School of Materials Science and Engineering, Beijing Advanced Innovation Center for Materials Genome Engineering, University of Science and Technology Beijing, Beijing 100083, China*

Yuanbo Wang − *School of Materials Science and Engineering, Beijing Advanced Innovation Center for Materials Genome Engineering, University of Science and Technology Beijing, Beijing 100083, China*

Jialong Liu − *Department of Physics and Electronics, School of Mathematics and Physics, Beijing University of Chemical Technology, Beijing 100029, China;* orcid.org/0000-0002-6072-1606

Jiawang Xu − *Anhui Key Laboratory of Magnetic Functional Materials and Devices, School of Materials Science and Engineering, Anhui University, Hefei 230601, China*

Tao Zhu − *Beijing National Laboratory for Condensed Matter Physics, Institute of Physics, Chinese Academy of Sciences, Beijing 100190, China*

Jie Qi − *School of Materials Science and Engineering, Beijing Advanced Innovation Center for Materials Genome Engineering, University of Science and Technology Beijing, Beijing 100083, China;* orcid.org/0000-0002-5105-9657

Xinqi Zheng − *School of Materials Science and Engineering, Beijing Advanced Innovation Center for Materials Genome Engineering, University of Science and Technology Beijing, Beijing 100083, China;* orcid.org/0000-0002-1894-4910

Yanfei Wu − *School of Materials Science and Engineering, Beijing Advanced Innovation Center for Materials Genome Engineering, University of Science and Technology Beijing, Beijing 100083, China;* orcid.org/0000-0002-2081-8091

Baogen Shen − *Beijing National Laboratory for Condensed Matter Physics, Institute of Physics, Chinese Academy of Sciences, Beijing 100190, China;* orcid.org/0000-0003-4819-1806

Complete contact information is available at:
https://pubs.acs.org/10.1021/acsami.3c12551

Author Contributions

[†]J.Z. and Y.Z. contributed equally to this paper.

Notes

The authors declare no competing financial interest.

◾ REFERENCES

(1) Liu, L.; Pai, C. F.; Li, Y.; Tseng, H. W.; Ralph, D. C.; Buhrman, R. A. Spin-torque switching with the giant spin Hall effect of Tantalum. *Science* **2012**, *336*, 555.

(2) Miron, I. M.; Garello, K.; Gaudin, G.; Zermatten, P. J.; Costache, M. V.; Auffret, S.; Bandiera, S.; Rodmacq, B.; Schuhl, A.; Gambardella, P. Perpendicular switching of a single ferromagnetic layer induced by in-plane current injection. *Nature* **2011**, *476*, 189.

(3) Qiu, X. P.; Narayanapillai, K.; Wu, Y.; Deorani, P.; Yang, D.; Noh, W.; Park, J.; Lee, K. J.; Lee, H. W.; Yang, H. Spin-orbit-torque engineering via oxygen manipulation. *Nat. Nanotechnol.* **2015**, *10*, 333.

(4) Cai, K. M.; Yang, M. Y.; Ju, H. L.; Wang, S. M.; Ji, Y.; Li, B. H.; Edmonds, K. W.; Sheng, Y.; Zhang, B.; Zhang, N.; Liu, S.; Zheng, H.; Wang, K. Y. Electric field control of deterministic current-induced magnetization switching in a hybrid ferromagnetic/ ferroelectric structure. *Nat. Mater.* **2017**, *16*, 712.

(5) Peng, S. Z.; Zhu, D. Q.; Li, W. X.; Wu, H.; Grutter, A. J.; Gilbert, D. A.; Lu, J. Q.; Xiong, D. R.; Cai, W. L.; Shafer, P.; Wang, K. L.; Zhao, W. S. Exchange bias switching in an antiferromagnet/ ferromagnet bilayer driven by spin-orbit torque. *Nat. Electronics* **2020**, *3*, 757.

(6) Xue, F.; Lin, S. J.; Song, M. Y.; Hwang, W.; Klewe, C.; Lee, C. M.; Turgut, E.; Shafer, P.; Vailionis, A.; Huang, Y. L.; Tsai, W.; Bao, X. Y.; Wang, S. X. Field-free spin-orbit torque switching assisted by in-plane unconventional spin torque in ultrathin $[Pt/Co]_N$. *Nat. Commun.* **2023**, *14*, 3932.

(7) Wang, H. Y.; Wu, H.; Zhang, J.; Liu, Y. J.; Chen, D. D.; Pandey, C.; Yin, J. L.; Wei, D. H.; Lei, N.; Shi, S. Y.; Lu, H. C.; Li, P.; Fert, A.; Wang, K. L.; Nie, T. X.; Zhao, W. S. Room temperature energy-efficient spin-orbit torque switching in two-dimensional van der Waals Fe_3GeTe_2 induced by topological insulators. *Nat. Commun.* **2023**, *14*, 5173.

(8) Dou, P. W.; Zhang, J. Y.; Guo, Y. Q.; Zhu, T.; Luo, J.; Zhao, G. P.; Huang, H.; Yu, G. Q.; Zhao, Y. C.; Qi, J.; Deng, X.; Wang, Y. B.; Li, J. L.; Shen, J. X.; Zheng, X. Q.; Wu, Y. F.; Yang, H. X.; Shen, B. G.; Wang, S. G. Deterministic magnetization switching via tunable noncollinear spin configurations in canted magnets. *Nano Lett.* **2023**, *23*, 6449.

(9) Fukami, S.; Anekawa, T.; Zhang, C.; Ohno, H. A spin-orbit torque switching scheme with collinear magnetic easy axis and current configuration. *Nat. Nanotechnol.* **2016**, *11*, 621.

(10) Zhang, J. Y.; Dou, P. W.; Peng, W. L.; Qi, J.; Liu, J. Q.; Liu, R. Y.; Zheng, X. Q.; Wu, Y. F.; Lyu, H. C.; Zhao, Y. C.; Zhu, Z. Z.; You, C. Y.; Kohn, A.; Wang, S. G. Enhanced spin-orbit torque switching in perpendicular multilayers via interfacial oxygen tunability. *Appl. Phys. Lett.* **2020**, *117*, 232406.

(11) Emori, S.; Bauer, U.; Ahn, S. M.; Martinez, E.; Beach, G. S. D. Current-driven dynamics of chiral ferromagnetic domain walls. *Nat. Mater.* **2013**, *12*, 611.

(12) Luo, S. J.; Tian, W. C.; Zhang, S.; Li, R. F.; Min, R.; Yang, X. F.; Zou, X. C.; Hong, J.; You, L. Integrator based on current-controlled magnetic domain wall. *Appl. Phys. Lett.* **2021**, *118*, 052402.

(13) Zahedinejad, M.; Mazraati, H.; Fulara, H.; Yue, J.; Jiang, S.; Awad, A. A.; Akerman, J. CMOS compatible W/CoFeB/MgO spin

Hall nano-oscillators with wide frequency tunability. *Appl. Phys. Lett.* **2018**, *112*, 132404.

(14) Fulara, H.; Zahedinejad, M.; Khymyn, R.; Awad, A. A.; Muralidhar, S.; Dvornik, M.; Akerman, J. Spin-orbit torque-driven propagating spin waves. *Sci. Adv.* **2019**, *5*, No. eaax8467.

(15) Zhu, L. J.; Zhang, X. S.; Muller, D. A.; Ralph, D. C.; Buhrman, A. Observation of strong bulk damping-like spin-orbit torque in chemically disordered ferromagnetic single layers. *Adv. Funct. Mater.* **2020**, *30*, 2005201.

(16) Qiu, X. P.; Legrand, W.; He, P.; Wu, Y.; Yu, J. W.; Ramaswamy, R.; Manchon, A.; Yang, H. Enhanced spin-orbit torque via modulation of spin current absorption. *Phys. Rev. Lett.* **2016**, *117*, 217206.

(17) Song, Y. H.; Zhao, X. T.; Liu, W.; Liu, L.; Li, S. K.; Zhang, Z. D. Spin-orbit torque driven four-state switching in splicing structure. *Appl. Phys. Lett.* **2020**, *117*, 232408.

(18) Xu, H.; Wei, J.; Zhou, H.; Feng, J.; Xu, T.; Du, H.; He, C.; Huang, Y.; Zhang, J.; Liu, Y.; Wu, H.-C.; Guo, C.; Wang, X.; Guang, Y.; Wei, H.; Peng, Y.; Jiang, W. J.; Yu, G. Q.; Han, X. F. High Spin Hall conductivity in large-area type-II Dirac semimetal PtTe$_2$. *Adv. Mater.* **2020**, *32*, 2000513.

(19) Ding, S. L.; Ross, A.; Go, D.; Baldrati, L.; Ren, Z. Y.; Freimuth, F.; Becker, S.; Kammerbauer, F.; Yang, J. B.; Jakob, G.; Mokrousov, Y.; Kläui, M. Harnessing orbital-to-spin conversion of interfacial orbital currents for efficient spin-orbit torques. *Phys. Rev. Lett.* **2020**, *125*, 177201.

(20) Dc, M.; Shao, D. F.; Hou, V. D. H.; Vailionis, A.; Quarterman, P.; Habiboglu, A.; Venuti, M. B.; Xue, F.; Huang, Y. L.; Lee, C. M.; Miura, M.; Kirby, B.; Bi, C.; Li, X.; Deng, Y.; Lin, S. J.; Tsai, W.; Eley, S.; Wang, W. G.; Borchers, J. A.; Tsymbal, E. Y.; Wang, S. X. Observation of anti-damping spin-orbit torques generated by in-plane and out-of-plane spin polarizations in MnPd$_3$. *Nat. Mater.* **2023**, *22*, 591.

(21) Oh, Y. W.; Chris Baek, S.; Kim, Y. M.; Lee, H. Y.; Lee, K. D.; Yang, C. G.; Park, E. S.; Lee, K. S.; Kim, K. W.; Go, G.; Jeong, J. R.; Min, B. C.; Lee, H. W.; Lee, K. J.; Park, B. G. Field-free switching of perpendicular magnetization through spin-orbit torque in antiferromagnet/ferromagnet/oxide structures. *Nat. Nanotechnol.* **2016**, *11*, 878.

(22) Chang, M. X.; Yun, J. J.; Zhai, Y. B.; Cui, B. S.; Zuo, Y. L.; Yu, G. Q.; Xi, L. Field free magnetization switching in perpendicularly magnetized Pt/Co/FeNi/Ta structure by spin orbit torque. *Appl. Phys. Lett.* **2020**, *117*, 142404.

(23) Shi, G. Y.; Wan, C. H.; Chang, Y. S.; Li, F.; Zhou, X. J.; Zhang, P. X.; Cai, J. W.; Han, X. F.; Pan, F.; Song, C. Spin-orbit torque in MgO/CoFeB/Ta/CoFeB/MgO symmetric structure with interlayer antiferromagnetic coupling. *Phys. Rev. B* **2017**, *95*, 104435.

(24) Ma, Q. L.; Li, Y. F.; Choi, Y.; Chen, W. C.; Han, S. J.; Chien, C. L. Spin orbit torque switching of synthetic Co/Ir/Co trilayers with perpendicular anisotropy and tunable interlayer coupling. *Appl. Phys. Lett.* **2020**, *117*, 172403.

(25) Xiong, D. R.; Peng, S. Z.; Lu, J.; Li, W. X.; Wu, H.; Li, Z.; Cheng, H. Y.; Wang, Y. Y.; Back, C. H.; Wang, K. L.; Zhao, W. S. Modulation of thermal stability and spin-orbit torque in IrMn/CoFeB/MgO structures through atom thick W insertion. *Appl. Phys. Lett.* **2020**, *117*, 212401.

(26) Tang, M.; Shen, K.; Xu, S. J.; Yang, H. L.; Hu, S.; Lü, W. M.; Li, C. J.; Li, M. S.; Yuan, Z.; Pennycook, S. J.; Xia, K.; Manchon, A.; Zhou, S. M.; Qiu, X. P. Bulk spin torque-driven perpendicular magnetization switching in $L1_0$ FePt single layer. *Adv. Mater.* **2020**, *32*, 2002607.

(27) Cao, Y.; Sheng, Y.; Edmonds, K. W.; Ji, Y.; Zheng, H. Z.; Wang, K. Y. Deterministic magnetization switching using lateral spin-orbit torque. *Adv. Mater.* **2020**, *32*, 1907929.

(28) Cui, B. H.; Wu, H.; Li, D.; Razavi, S. A.; Wu, D.; Wong, K. L.; Chang, M. X.; Gao, M. Z.; Zuo, Y. L.; Xi, L.; Wang, K. L. Field-free spin-orbit torque switching of perpendicular magnetization by the Rashba interface. *ACS Appl. Mater. Interfaces* **2019**, *11*, 39369.

(29) Razavi, A.; Wu, H.; Shao, Q. M.; Fang, C.; Dai, B. Q.; Wong, K.; Han, X. F.; Yu, G. Q.; Wang, K. L. Deterministic spin-orbit torque switching by a light-metal insertion. *Nano Lett.* **2020**, *20*, 3703.

(30) Liu, L.; Zhou, C. H.; Shu, X. Y.; Li, C. J.; Zhao, T. Y.; Lin, W. N.; Deng, J. Y.; Xie, Q. D.; Chen, S. H.; Zhou, J.; Guo, R.; Wang, H.; Yu, J. H.; Shi, S.; Yang, P.; Pennycook, S.; Manchon, A.; Chen, J. S. Symmetry-dependent field-free switching of perpendicular magnetization. *Nat. Nanotechnol.* **2021**, *16*, 277.

(31) Filianina, M.; Hanke, J. P.; Lee, K.; Han, D. S.; Jaiswal, S.; Rajan, A.; Jakob, G.; Mokrousov, Y.; Kläui, M. Electric-field control of spin-orbit torques in perpendicularly magnetized W/CoFeB/MgO films. *Phys. Rev. Lett.* **2020**, *124*, 217701.

(32) Mishra, R.; Mahfouzi, F.; Kumar, D.; Cai, K. M.; Chen, M. J.; Qiu, X. P.; Kioussis, N.; Yang, H. Electric-field control of spin accumulation direction for spin-orbit torques. *Nat. Commun.* **2019**, *10*, 248.

(33) Liu, L. Q.; Chen, C. T.; Sun, J. Z. Spin Hall effect tunnelling spectroscopy. *Nat. Phys.* **2014**, *10*, 561.

(34) Pai, C. F.; Liu, L. Q.; Li, Y.; Tseng, H. W.; Ralph, D. C.; Buhrman, R. A. Spin transfer torque devices utilizing the giant spin Hall effect of tungsten. *Appl. Phys. Lett.* **2012**, *101*, 122404.

(35) Fert, A.; Levy, P. M. Spin Hall effect induced by resonant scattering on impurities in metals. *Phys. Rev. Lett.* **2011**, *106*, 157208.

(36) Niimi, Y.; Kawanishi, Y.; Wei, D. H.; Deranlot, C.; Yang, H. X.; Chshiev, M.; Valet, T.; Fert, A.; Otani, Y. Giant spin Hall effect induced by skew scattering from bismuth impurities inside thin film CuBi alloys. *Phys. Rev. Lett.* **2012**, *109*, 156602.

(37) Dc, M.; Grassi, R.; Chen, J. Y.; Jamali, M.; Reifsnyder Hickey, D.; Zhang, D. L.; Zhao, Z. Y.; Li, H. S.; Quarterman, P.; Lv, Y.; Li, M.; Manchon, A.; Mkhoyan, K. A.; Low, T.; Wang, J. P. Room-temperature high spin-orbit torque due to quantum confinement in sputtered Bi$_x$Se$_{(1-x)}$ films. *Nat. Mater.* **2018**, *17*, 800.

(38) Wu, H.; Xu, Y.; Deng, P.; Pan, Q. J.; Razavi, S. A.; Wong, K.; Huang, L.; Dai, B. Q.; Shao, Q. M.; Yu, G. Q.; Han, X. F.; Rojas-Sánchez, J. C.; Mangin, S.; Wang, K. L. Spin-orbit torque switching of a nearly compensated ferrimagnet by topological surface states. *Adv. Mater.* **2019**, *31*, 1901681.

(39) Wu, H.; Zhang, P.; Deng, P.; Lan, Q. Q.; Pan, Q. J.; Razavi, S. A.; Che, X. Y.; Huang, L.; Dai, B. Q.; Wong, K.; Han, X. F.; Wang, K. L. Room-temperature spin-orbit torque from topological surface states. *Phys. Rev. Lett.* **2019**, *123*, 207205.

(40) Ikeda, S.; Miura, K.; Yamamoto, H.; Mizunuma, K.; Gan, H. D.; Endo, M.; Kanai, S.; Hayakawa, J.; Matsukura, F.; Ohno, H. A perpendicular-anisotropy CoFeB-MgO magnetic tunnel junction. *Nat. Mater.* **2010**, *9*, 721.

(41) Cecot, M.; Karwacki, L.; Skowronski, W.; Kanak, J.; Wrona, J.; Zywczak, A.; Yao, L.; van Dijken, S. V.; Barnas, J.; Stobiecki, T. Influence of intermixing at the Ta/CoFeB interface on spin Hall angle in Ta/CoFeB/MgO heterostructures. *Sci. Rep.* **2017**, *7*, 968.

(42) Haney, P. M.; Lee, H. W.; Lee, K. J.; Manchon, A.; Stiles, M. D. Current induced torques and interfacial spin-orbit coupling: Semi-classical modeling. *Phys. Rev. B* **2013**, *87*, 174411.

(43) Rojas-Sanchez, J. C.; Reyren, N.; Laczkowski, P.; Savero, W.; Attane, J. P.; Deranlot, C.; Jamet, M.; George, J. M.; Vila, L.; Jaffres, H. Spin pumping and inverse spin Hall effect in platinum: the essential role of spin-memory loss at metallic interfaces. *Phys. Rev. Lett.* **2014**, *112*, 106602.

(44) Zhu, L. J.; Buhrman, R. A. Maximizing spin-orbit-torque efficiency of Pt/Ti Multilayers: Trade-off between intrinsic spin Hall conductivity and carrier lifetime. *Phys. Rev. Appl.* **2019**, *12*, 051002.

(45) Han, X. F.; Wang, X.; Wan, C. H.; Yu, G. Q.; Lv, X. R. Spin-orbit torques: Materials, physics, and devices. *Appl. Phys. Lett.* **2021**, *118*, 120502.

(46) Zhang, J. Y.; Zhang, Y.; Gao, Y.; Zhao, G. P.; Qiu, L.; Wang, K. Y.; Dou, P. W.; Peng, W. L.; Zhuang, Y.; Wu, Y. F.; Yu, G. Q.; Zhu, Z. Z.; Zhao, Y. C.; Guo, Y. Q.; Zhu, T.; Cai, J. W.; Shen, B. G.; Wang, S. G. Magnetic skyrmions in a hall balance with interfacial canted magnetizations. *Adv. Mater.* **2020**, *32*, 1907452.

(47) Kresse, G.; Furthmuller, J. Efficient iterative schemes for ab initio total-energy calculations using a plane-wave basis set. *Phys. Rev. B* **1996**, *54*, 11169.

(48) Ernzerhof, M.; Scuseria, G. E. Assessment of the Perdew-Burke-Ernzerhof exchange-correlation functional. *J. Chem. Phys.* **1999**, *110*, 5029.

(49) Hammer, B.; Hansen, L. B.; Norskov, J. K. Improved adsorption energetics within density-functional theory using revised Perdew-Burke-Ernzerhof functionals. *Phys. Rev. B* **1999**, *59*, 7413.

(50) Huang, H.; Wu, H.-H.; Chi, C.; Huang, B.; Zhang, T.-Y. Ab initio investigations of orthogonal ScC_2 and ScN_2 monolayers as promising anode materials for sodium-ion batteries. *J. Mater. Chem. A* **2019**, *7*, 8897.

(51) Peng, W. L.; Zhang, J. Y.; Feng, G. N.; Xu, X. L.; Yang, C.; Jia, Y. L.; Yu, G. H. Enhancement of spin-orbit torque via interfacial hydrogen and oxygen ion manipulation. *Appl. Phys. Lett.* **2019**, *115*, 092402.

(52) Liu, L. Q.; Moriyama, T.; Ralph, D. C.; Buhrman, R. A. Spin-torque ferromagnetic resonance induced by the spin Hall effect. *Phys. Rev. Lett.* **2011**, *106*, 036601.

(53) He, P.; Qiu, X. P.; Zhang, V. L.; Wu, Y.; Kuok, M. H.; Yang, H. Continuous tuning of the magnitude and direction of spin-orbit torque using bilayer heavy metals. *Adv. Electron. Mater.* **2016**, *2*, 1600210.

(54) Zhu, L. J.; Buhrman, R. A. Absence of significant spin-current generation in Ti/Fe-Co-B bilayers with strong interfacial spin-orbit coupling. *Phys. Rev. Appl.* **2021**, *15*, L031001.

(55) Choi, Y. G.; Jo, D.; Ko, K. H.; Go, D.; Kim, K. H.; Park, H. G.; Kim, C.; Min, B. C.; Choi, G. M.; Lee, H. W. Observation of the orbital Hall effect in a light metal Ti. *Nature* **2023**, *52*, 619.

(56) Zhang, J. Y.; Dou, P. W.; Zhao, Y. C.; Zhang, S. L.; Liu, J. Q.; Qi, J.; Lyu, H. C.; Liu, R. Y.; Yu, G. H.; Jiang, Y.; Shen, B. G.; Wang, S. G. Multi-field manipulation in Hall balance. *Acta Phys. Sin.* **2021**, *70*, 048501.

(57) Ikeda, S.; Hayakawa, J.; Ashizawa, Y.; Lee, Y. M.; Miura, K.; Hasegawa, H.; Tsunoda, M.; Matsukura, F.; Ohno, H. Tunnel magnetoresistance of 604% at 300 K by suppression of Ta diffusion in CoFeB/MgO/CoFeB pseudo-spin-valves annealed at high temperature. *Appl. Phys. Lett.* **2008**, *93*, 082508.

(58) Chen, Y. F.; Zhang, Q. H.; Jia, J. X.; Zheng, Y. Q.; Wang, Y.; Fan, X. L.; Cao, J. W. Tuning Slonczewski-like torque and Dzyaloshinskii-Moriya interaction by inserting a Pt spacer layer in Ta/CoFeB/MgO structures. *Appl. Phys. Lett.* **2018**, *112*, 232402.

(59) Li, S. K.; Zhao, X. T.; Liu, W.; Zhao, X. G.; Zhang, Z. D. Modulation of spin-orbit torque induced magnetization switching in Pt/CoFe through oxide interlayers. *Appl. Phys. Lett.* **2019**, *114*, 212404.

(60) Ma, X.; Yu, G. Q.; Tang, C.; Li, X.; He, C. L.; Shi, J.; Wang, K. L.; Li, X. Q. Interfacial Dzyaloshinskii-Moriya interaction: effect of 5d band filling and correlation with spin mixing conductance. *Phys. Rev. Lett.* **2018**, *120*, 157204.

(61) Soumyanarayanan, A.; Reyren, N.; Fert, A.; Panagopoulos, C. Emergent phenomena induced by spin-orbit coupling at surfaces and interfaces. *Nature* **2016**, *539*, 509.

(62) Lee, O. J.; Liu, L. Q.; Pai, C. F.; Li, Y.; Tseng, H. W.; Gowtham, P. G.; Park, J. P.; Ralph, D. C.; Buhrman, R. A. Central role of domain wall depinning for perpendicular magnetization switching driven by spin torque from the spin Hall effect. *Phys. Rev. B* **2014**, *89*, 024418.

(63) Khvalkovskiy, A. V.; Cros, V.; Apalkov, D.; Nikitin, V.; Krounbi, M.; Zvezdin, K. A.; Anane, A.; Grollier, J.; Fert, A. Matching domain-wall configuration and spin-orbit torques for efficient domain-wall motion. *Phys. Rev. B* **2013**, *87*, 020402.

(64) Nguyen, M. H.; Ralph, D. C.; Buhrman, R. A. Spin torque study of the spin Hall conductivity and spin diffusion length in platinum thin films with varying resistivity. *Phys. Rev. Lett.* **2016**, *116*, 126601.

(65) Mukherjee, S.; Knut, R.; Mohseni, S. M.; Anh Nguyen, T. N.; Chung, S.; Tuan Le, Q.; Akerman, J.; Persson, J.; Sahoo, A.; Hazarika, A.; Pal, B.; Thiess, S.; Gorgoi, M.; Anil Kumar, P. S.; Drube, W.; Karis, O.; Sarma, D. D. Role of boron diffusion in CoFeB/MgO magnetic tunnel junctions. *Phys. Rev. B* **2015**, *91*, 085311.

(66) Zhai, H. Y.; Christen, H. M.; Cantoni, C.; Goyal, A.; Lowndes, D. H. Epitaxial titanium diboride films grown by pulsed-laser deposition. *Appl. Phys. Lett.* **2002**, *80*, 1963.

(67) Liu, F. Y.; Sun, K.; Li, W.; Yan, C.; Cui, H.; Jiang, L.; Hao, X.; Green, M. A. Enhancing the Cu_2ZnSnS_4 solar cell efficiency by back contact modification: Inserting a thin TiB_2 intermediate layer at Cu_2ZnSnS_4/Mo interface. *Appl. Phys. Lett.* **2014**, *104*, 051105.

(68) Zhang, W.; Han, W.; Jiang, X.; Yang, S. H.; Parkin, S. S. P. Role of transparency of platinum-ferromagnet interfaces in determining the intrinsic magnitude of the spin Hall effect. *Nat. Phys.* **2015**, *11*, 496.

(69) Qiu, Z.; Ando, K.; Uchida, K.; Kajiwara, Y.; Takahashi, R.; Nakayama, H.; An, T.; Fujikawa, Y.; Saitoh, E. Spin mixing conductance at a well-controlled platinum/ yttrium iron garnet interface. *Appl. Phys. Lett.* **2013**, *103*, 092404.